Aerosol optics model for black carbon applicable to remote sensing, chemical data assimilation, and climate modelling

Downloaded from: https://research.chalmers.se, 2026-04-05 11:00 UTC

Citation for the original published paper (version of record):
Kahnert, M., Kanngiesser, F. (2021). Aerosol optics model for black carbon applicable to remote sensing, chemical data assimilation,
and climate modelling. Optics Express, 29(7): 10639-10658. http://dx.doi.org/10.1364/OE.422523

N.B. When citing this work, cite the original published paper.

research.chalmers.se offers the possibility of retrieving research publications produced at Chalmers University of Technology. It covers all kind of research output: articles, dissertations, conference papers, reports etc. since 2004. research.chalmers.se is administrated and maintained by Chalmers Library

(article starts on next page)

Research Article Vol. 29, No. 7 / 29 March 2021 / Optics Express 10639
Optics EXPRESS

Aerosol optics model for black carbon applicable to remote sensing, chemical data assimilation, and climate modelling

MICHAEL KAHNERT[1,2,*] AND FRANZ KANNGIEßER[2]

[1]Research Department, Swedish Meteorological and Hydrological Institute, Folkborgsvägen 17, 60176 Norrköping, Sweden
[2]Department of Space, Earth and Environment, Chalmers University of Technology, Maskingränd 2, 41296 Gothenburg, Sweden
[*]michael.kahnert@smhi.se

Abstract: Aerosol optics models are an integral part of of climate models and of retrieval methods for global remote sensing observations. Such large-scale environmental applications place tight constraints on the affordable model complexity, which are difficult to reconcile with the considerable level of detail that is needed to capture the sensitivity of optical properties to morphological aerosol characteristics. Here, we develop a novel core-grey-shell dimer model and demonstrate its potential for reproducing radiometric and polarimetric properties of black carbon aerosols. The depolarisation is mainly sensitive to the relative size of the monomers, while the optical cross sections depend on the core-shell partitioning of black carbon. The optimum choice of these parameters is fairly stable across particle sizes and soot volume fraction, as is demonstrated by comparison with a more realistic coated aggregate model.

© 2021 Optical Society of America under the terms of the OSA Open Access Publishing Agreement

1. Introduction

Black carbon (BC) aerosols are among the primary anthropogenic air pollutants that contribute to radiative heating of the climate system by absorption of visible solar radiation [1–3]. Also, BC is a public health issue, as elevated concentrations of this aerosol in ambient air can cause pulmonary and cardiovascular diseases [4]. Thus, measures to reduce BC emissions improve air quality, while simultaneously helping to slow down global warming on a short time-scale.

Understanding the light-scattering properties of BC aggregates serves three important purposes. (i) It lays the foundation for quantifying the radiative impact of atmospheric BC aerosols on the climate system [5–8]. (ii) It provides the scientific basis for interpreting remote sensing observations of BC, which allows us to monitor the global distribution, transport pathways, and long-term trends of aerosol emissions. (iii) Related to this, it allows us to construct aerosol-optics observation operators for chemical data assimilation, which is the prerequisite for constraining air-quality forecasting models with remote-sensing data.

Efforts to model the optical properties from first principles are encumbered by the high morphological complexity of these types of aerosols [9–13]. The particles are typically composed of BC monomers that form irregular fractal aggregates, which are subsequently coated by more volatile material, such as sulphate [14–17], organic substances [16–19], salt [15], and water [20–23]. The challenge in optical modelling is to disentangle the impacts of these various features on the optical properties. Substantial efforts have been invested into studying the significance of the BC aggregates' monomer size [24], monomer polydispersity [25–29], monomer shape [30], overlapping and necking of monomers [29,31–36], fractal dimension [7,26], and internal mixing with volatile material [16,37–44].

For uncoated BC particles, our understanding of the relation between morphological subtleties and optical properties has reached a high degree of maturity. In a recent article, substantial

#422523 https://doi.org/10.1364/OE.422523
Journal © 2021 Received 11 Feb 2021; revised 12 Mar 2021; accepted 13 Mar 2021; published 19 Mar 2021

Optics EXPRESS

progress has been made toward discerning some general patterns from a mass of detail reported in earlier studies [36]. The authors investigated monomer polydispersity, irregular shapes, thin coatings, as well as necking and overlapping; they showed that much of the effect of these minor morphological features on optical cross sections derives from their effect on the particle volume. After applying an appropriate scaling transformation based on particle volume, the remaining effect of these morphological features is remarkably small — on the order of 5 % — which can be accounted for by an appropriate bias correction. The conclusion is that optical properties of uncoated BC aerosols can be well described, with appropriate corrections, by a model of fractal aggregates composed of monodisperse spherical monomers in point-contact with each other. Such a model is relatively efficient, and it is feasible to apply it to large-scale applications [6,45], such as chemical data assimilation, climate modelling, and remote sensing.

Coating of BC aggregates by volatile substances adds substantial complexity to the problem. Models with various assumptions about the composition and shape of the coating have been devised [28,30,38–40,43,46–54]. The most important insights that have emerged from recent studies can be summarized as follows [9].

- The absorption cross section C_{abs} of coated BC aggregates is strongly impacted by how much the monomers in the aggregate shield one another from interacting with the electromagnetic field [7]. The stronger this shielding effect, the less BC mass contributes to absorption, the lower C_{abs}. The conventional concentric core-shell model overestimates the shielding effect, because it tightly packs the entire BC mass in a massive spherical core, while in a realistic aggregate the BC mass is distributed in a more lacy structure [38,55]. By contrast, in the homogeneous grey-sphere model the entire BC mass is homogeneously mixed with the coating material, resulting in an underestimation of the shielding effect, which causes an overestimation of C_{abs}. Based on this understanding, a simple core-grey-shell (CGS) model has been devised [39], in which only part of the BC mass is concentrated in a spherical core, while the rest of the BC mass is homogeneously mixed with the weakly absorbing coating material in a concentric spherical shell. The partitioning of the BC mass between the core and the shell is a free tuning parameter of the model that allows us to tune the degree of shielding, thus the absorption cross section (as well as other optical properties) over a considerable range. The CGS model includes the conventional core-shell and the homogeneous grey-sphere models as limiting cases.

- The linear backscatter depolarisation ratio δ_{l} of coated BC aggregates requires the use of nonspherical model geometries, since spherically symmetric particles yield $\delta_{\mathrm{l}} = 0$ owing to symmetry. The main morphological property that determines δ_{l} is the shape of the coating material [40,41]. The morphology of the aggregate has, at least for thick coatings, a minor impact. Based on this notion, a model has been developed that allows us to tune how quickly the coating shell reaches spherical shape as more coating material is being added to the aggregate [41,42]. This model makes use of a single tuning parameter, while covering a considerable range of depolarisation ratios [9].

These two models have very different computational requirements. The CGS model is highly symmetric and can be run with extended Mie programs for concentric core-mantel spheres. The computations are very fast, which makes this model suitable for building extensive look-up tables for large-scale applications. It has recently been used for setting up the aerosol-optics observation operator in a chemical data assimilation system [56,57]. By contrast, the tunable coating model describes a morphologically realistic irregular geometry that can only be used in conjunction with very general and computationally demanding numerical methods for solving the light-scattering problem. Thus we currently lack a computationally inexpensive model for simulating differential polarimetric properties of coated BC aggregates. This is a considerable gap in our modelling

Optics EXPRESS

capabilities that impedes our capacity to exploit polarimetric data, such as lidar observations of the depolarisation ratio. The goal of this study is to develop a model that can fill this gap.

More specifically, the aim is to find a model with which we can simultaneously simulate the optical cross sections and the linear depolarisation ratio. The idea is to construct a geometrically simple model that incorporates the main physical insights on which the CGS model [39] and the irregular coated aggregate model [41] are based. Thus the main hypothesis is that the essential model capabilities are to account for the shielding effect as well as for the geometry's impact on depolarization. The main result of our investigation is that this can be accomplished with a simple CGS dimer.

There are other efforts to model optical properties with simple model geometries. For instance, in [58] both spheroids and Chebyshev particles were employed for constructing look-up tables of the lidar ratio and the linear backscatter depolarization ratio. The refractive index is often a free parameter in such look-up tables. Here, we specifically aim at developing a simple model that is not limited to lidar retrievals, but comprises a broader range of applications. This is particularly important for chemical transport models (CTMs) for the following reasons. (i) Chemical data assimilation makes use of different types of measurements from different instruments, such as backscattering coefficient, depolarisation ratio, and aerosol optical depth. (ii) CTMs can be coupled to general circulation models (e.g. [59]), which requires the computation of climate-relevant aerosol optical properties, such as extinction coefficient and single scattering albedo. (iii) The refractive index is directly related to the chemical composition of the aerosols, which is one of the main prognostic variables of the CTM. Thus, we do not have the liberty of treating this quantity as a free parameter, as is often done in retrieval look-up tables. Rather, we need an optics model for coated soot particles in which the refractive index is related in a consistent way to the chemical composition of the particles. Based on these requirements, we are looking for a model that allows us to simultaneously simulate depolarization as well as extinction, absorption, and backscattering cross sections, with the constraint that the refractive index needs to be consistent with the chemical composition of the particles.

The model particles as well as the computational methodology will be explained in Sec. 2. The main results are presented and discussed in Secs. 3 and 4, respectively. Concluding remarks are found in Sec. 5.

2. Methods

2.1. Model particles

All computations are performed for a wavelength of λ=532nm, which is frequently employed in lidar instruments. For BC we assume a refractive index of m_{BC}=1.763+0.632i, which is based on measurements reported in [60]. The coating is assumed to be sulfate with a refractive index m_{SO4}=1.43+10^{-8}i [61].

2.1.1. Reference model

We employ the tunable coated aggregate model introduced in [41] as a reference model. This model is capable of systematically producing a wide variety of realistic aerosol morphologies. The particles are constructed according to the following steps.

- First, we prescribe the number N_{s} of BC monomers, the monomer radius a, the aggregate's fractal dimension D_{f} and fractal prefactor k_0, as well as the total volume-equivalent radius R_{v} of the coated aggregate. This fixes the volume fraction f_{BC} of BC in the particle.
- Next, a bare BC aggregate is formed by use of the cluster aggregation algorithm developed in [62]. In each step of the pseudo-random aggregation process, the aggregate satisfies the

Optics EXPRESS

scaling relation

$$N_s = k_0 \left(\frac{R_g}{a}\right)^{D_f}, \tag{1}$$

where the radius of gyration is defined by

$$R_g = \sqrt{\frac{1}{N_s}\sum_{i=1}^{N_s}(r_i - r_c)^2}, \tag{2}$$

r_i denotes the position of the center of mass of the ith monomer, and r_c is the position of the center of mass of the aggregate.

- Let the smallest circumscribing sphere that encloses the aggregate have diameter D_0, and let the center of that sphere be positioned at r_s. We imagine that we scale that sphere by a factor f_c. We call the diameter $D_c = f_c D_0$ the critical diameter. Next, we apply the coating material to the aggregate layer by layer with a coating thickness d, starting from those monomers that are closest to the center r_s of the circumscribing sphere. However, we constrain the application of the coating material to lie inside the critical sphere. This process is continued until the required amount of coating material is applied, i.e., until the coated aggregate has reached the prescribed size R_v or, equivalently, until the BC volume fraction has reached the prescribed value f_{BC}.

- If all empty space inside the critical sphere is completely filled up, but the required coating amount has not yet been applied, then from this point on the remaining coating material is added concentrically in spherical layers of thickness d onto the critical sphere.

The scaling factor f_c is the free tuning parameter in this model. The smaller the size of the critical sphere, the faster the coating process results in a spherical mantel. The idea is to adjust the shape of the coating in order to tune the depolarisation ratio, which is highly sensitive to exactly this morphological property.The model is well adapted to be used in the discrete dipole approximation (DDA, see Sec. 2.2), where the coating thickness d in the model is set equal to the dipole spacing in the DDA.

Reference computations have been performed for the particles illustrated in Fig. 1. We considered two particle sizes, R_v=542nm (rows 1-2) and 280nm (rows 3-4). For each size, we considered two BC volume fractions, f_{BC}=0.07 (rows 1 and 3) and 0.20 (rows 2 and 4). The lower value is more typical for aged, long-range transported BC aerosols (e.g. [17]), while the higher value is closer to what one would find in BC aerosols in proximity to the emission sources (e.g. [16]). As aged BC aggregates tend to be more compact than freshly emitted aggregates, we assumed a fractal dimension D_f=2.6 for the particles with f_{BC}=0.07 (rows 1 and 3), and D_f=2.4 for f_{BC}=0.20 (rows 2 and 4). In either case we used a fractal prefactor k_0=0.7.

For each of the four instances of (R_v,f_{BC}), we constructed model particle with four different values of the model's tuning parameter, namely f_c=0.5, 0.7, 0.8, and 0.95, as labeled in the figure. The effect of f_c on the shape of the coating depends on the volume fraction. For low *BC* volume fractions (rows 1 and 3), a large amount of coating material is applied, which is likely to completely fill up the critical sphere unless a fairly high value of the critical radius is chosen. Thus we obtain coatings that significantly deviate from spherical shape only for f_c=0.95. By contrast, for higher BC volume fractions (rows 2 and 4), the correspondingly small amount of coating material is hardly enough to fill up the critical sphere. Thus, only for f_c=0.5 the coating approaches spherical shape. For f_c>0.7 the coating more or less follows the shape of the aggregate.

For each of the 16 types of particles shown in Fig. 1, five stochastic realisations of the aggregate geometry were generated. Also, in the absence of a priori information about the shape of

Optics EXPRESS

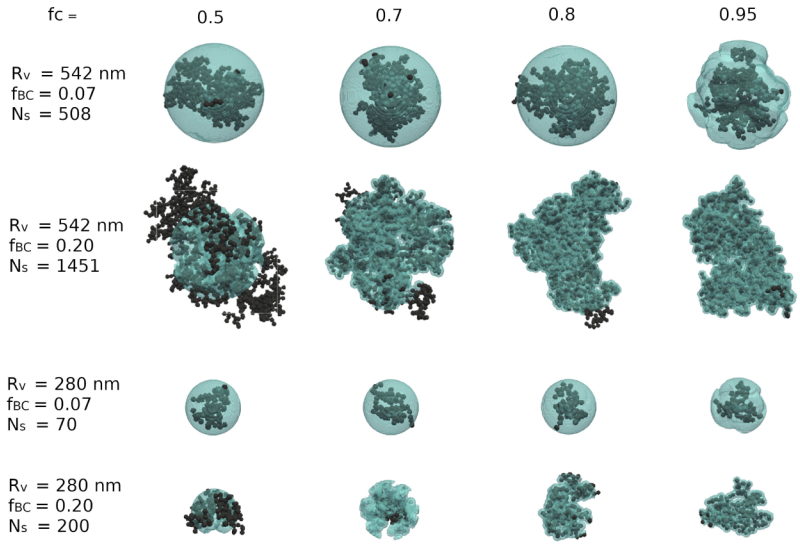

Fig. 1. Reference model of coated BC aggregates. The volume-equivalent sizes are R_v=542nm (rows 1–2) and 280nm (rows 3–4), the BC volume fractions are f_{BC}=0.07 (rows 1, 3) and 0.20 (rows 2, 4). The scaling factor f_c of the critical radius in the model in columns 1–4 is 0.5, 0.7, 0.8, and 0.95, respectively. The figure shows only one out of five stochastic realisations of each model geometry.

the coating, we do not know which value of f_c is most realistic. Therefore, we averaged the computational results over the four values of f_c, as well as over the five pseudo-random geometries. Thus, for each of the four instances of (R_v, f_{BC}) we obtain mean optical properties averaged over an ensemble consisting of 20 different geometries.

2.1.2. Aggregate partially embedded in spherical coating

The reference model can only be used in conjunction with computationally demanding numerical light-scattering methods, such as the DDA [63]. One goal of this paper is to test models that can be used in conjunction with the multiple sphere T matrix (MSTM) method [64], which is generally faster. However, this method is limited to geometries consisting of spherical monomers with non-overlapping surfaces.

Here we test a model geometry that was first proposed in [48]. In that model the soot aggregate is semi-embedded in a spherical mantel, while making sure that none of the BC monomers overlaps with the spherical shell. In [48] this model was studied by simulating optical cross sections and the asymmetry parameter. Here, we want to investigate the model with an emphasis on differential radiometric and polarimetric properties relevant to lidar remote sensing.

The construction of the particles proceeds as follows.

- First we prescribe the properties of the fractal aggregate (N_s, a, D_f, k_0), as well as the total particle size R_v (or, equivalently, the BC volume fraction f_{BC}). We further prescribe the number Ns^{inside} of BC monomers that are embedded in the coating material. This determines the radius R_{coat} of the coating sphere. More specifically, the total volume of the particle is
$$\frac{4}{3}\pi R_v^3 = (Ns - Ns^{inside})\frac{4}{3}\pi a^3 + \frac{4}{3}\pi R_{coat}^3, \tag{3}$$
which can be solved for R_{coat}.

Optics EXPRESS

- The construction starts by placing two monomers on either side of the surface of the coating sphere of radius R_{coat}, such that all three spheres touch in a single point. Then more monomers are added both inside and outside the coating, until a total of N_s^{inside} are embedded by the coating sphere, and ($N_s - N_s^{inside}$) are attached outside that sphere. The monomers both inside and outside are added at pseudo-random positions but under the constraint that the fractal scaling relation given in Eq. (1) be satisfied in each step of the process. The inside spheres have to fulfill the additional constraint that they be fully embedded, i.e., they may share at most a single point with the surface of the coating sphere. The diffusion-limited aggregation algorithm was used for assembling the aggregates [65].

Figure 2 illustrates three representative geometries with a variable number N_s^{inside}. We performed calculations for a particle with volume-equivalent radius R_v=542nm, BC volume fraction f_{BC}=0.07, and for aggregates with N_s=508, a=28nm, D_f=2.6, and k_0=0.7. Thus the fractal characteristics are equivalent to those used in the corresponding reference model. The free parameter, i.e., the number of monomers inside the coating, was varied by considering the values N_s^{inside}=1, 51, 101, 152, 203, 254, 304, 355, 406, 456, and 507. For each value of N_s^{inside}, five stochastic realizations of the geometry were generated.

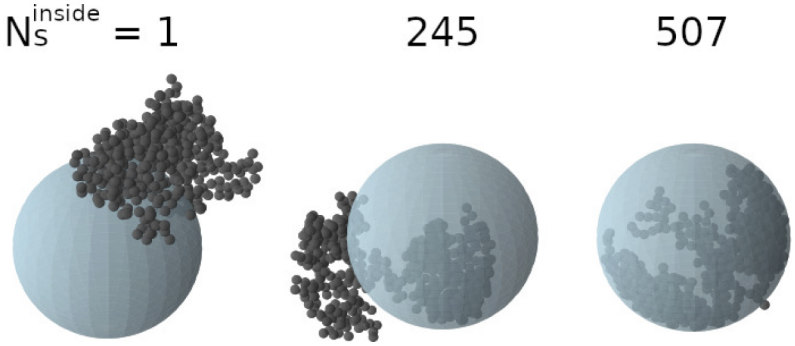

Fig. 2. Model of partially embedded BC aggregates with non-overlapping monomers, illustrated for a particle with a BC volume fraction of f_{BC}=0.07. The aggregate contains a total of N_s=508 monomers, and the number of monomers inside the spherical mantel, N_s^{inside}, increases from left to right.

In this model the BC monomers and the coating are spherical, and none of the spherical surfaces overlap. Thus, this class of geometry can be used in conjunction with the MSTM method (see Sec. 2.2). However, we also suspect that the sphericity of the coating limits the range of depolarisation ratios that can be simulated with this model. The main question is if the non-sphericity owing to the protruding BC aggregate can make up for this. Thus, we hypothesize that an increase in N_s^{inside}, which makes the overall shape more spherical, should result in a decrease in the depolarisation ratio. We want to find out within what range we can tune the depolarisation ratio by varying the free parameter N_s^{inside} of the model.

2.1.3. Core-grey-shell dimer (CGS2) model

The model presented in the previous section suffers from two main drawbacks. (i) The geometry is still relatively complex, which may limit its applicability to large-scale applications. (ii) The coating is spherical, which is likely to limit the range of depolarisation ratios that can be simulated with this model. We now want to overcome these limitations. In particular, based on what we learned in earlier studies [9,40,41], we expect that the nonsphericity of the coating is the decisive morphological feature that impacts the depolarisation ratio. Thus we want to devise a simple model with a non-spherical coating.

Optics EXPRESS

We further know that the core-grey-shell (CGS) model allows us to tune the optical cross sections over a considerable range. [9,39]. This model is based on a concentric spherical core-shell geometry. However, unlike in the conventional core-shell model, only a fraction f_{core} of the BC mass is concentrated in the core, while the remaining fraction $(1-f_{\mathrm{core}})$ is homogeneously mixed with the material of the shell. The effective refractive index of the shell is computed by use of effective medium theory (e.g. [66]). The lower the core fraction f_{core}, the more "grey" the shell becomes, i.e., the mantel becomes more absorbing owing to the higher BC content. The idea behind this simple model is to mimic how the BC mass in a realistic aggregate can be distributed in a more compact or a more lacy structure, depending on the fractal dimension. However, the refractive indices of the core and the mantle are *not* free parameters of the model. Once the tuning parameter f_{core} has been fixed, the refractive index of the mantle is unambiguously determined by the chemical composition of the particle. This is an essential prerequisite for applying the model to chemical data assimilation.

The CGS model is spherical, hence unsuitable for modeling depolarisation. Our objective is to devise a nonspherical version of the CGS model that will allow us to tune both the cross sections (by modifying f_{core}) and the depolarisation ratio (by varying the degree of nonsphericity). An obvious way to do that would be to distort the spherical CGS geometry into a spheroidal geometry. The main obstacle is that we currently lack a fast numerical method, especially a T-matrix based method, for computing core-shell spheroids with an absorbing mantel. Note that in [67] a fast T-matrix method for core-mantel axially symmetric particles was presented, but only for non-absorbing coatings.

Based on these considerations, we propose the following model. Rather than putting the entire particle mass into a single CGS particle, we divide up the mass into two, in general unequal parts and form two core-grey-shell particles, which we assemble into a dimer. More specifically, let R_{v} be the volume-equivalent radius of the entire particle consisting of BC and the coating material. We denote the BC volume fraction by $f_{\mathrm{BC}} = V_{\mathrm{BC}}/V_{\mathrm{tot}}$, where V_{BC} is the BC volume in the particle, and $V_{\mathrm{tot}} = 4\pi R_{\mathrm{v}}^3/3$ is the total particle volume. We form a CGS sphere with the same volume fraction f_{BC}, but with a volume-equivalent radius $R_1 \leq R_{\mathrm{v}}$, and a second CGS sphere with radius R_2 such that $R_1^3 + R_2^3 = R_{\mathrm{v}}^3$, i.e., $V_1 + V_2 = V$, where V_1 and V_2 are the volumes of the first and second CGS particle, respectively. Finally, the two CGS monomers are assembled into a dimer. The model has two free parameters, as illustrated in Fig. 3.

The first parameter is the relative size of the CGS constituents, which we express by R_1/R_{v}. For R_1/R_{v}=0.794, we have $(R_1/R_{\mathrm{v}})^3$=0.5, i.e., the two CGS spheres in the dimer have equal volume (left column). For R_1/R_{v}=1, the first CGS sphere contains all of the particle volume, i.e., the second CGS sphere has vanished, and we recover the conventional CGS model (right column). By adjusting R_1/R_{v} between 0.794 and 1 we can vary the nonspherical geometry of the model. We hypothesize that this will allow us to simulate a wide range of depolarisation ratios. For brevity, we will refer to this CGS dimer as the CGS2 model.

The second parameter is the core fraction f_{core}. For $f_{\mathrm{core}} = 1$, all of the BC mass is concentrated in the cores of each of the two CGS monomers (top row). For $f_{\mathrm{core}} = 0$, the core has vanished and all of the BC mass is homogeneously mixed with the coating material. By adjusting f_{core} we can make the shell more or less absorbing, which is represented in the figure by varying color shades. We hypothesize that this will allow us to adjust the optical cross sections in a similar way as in the conventional spherical CGS model.

Microphysically, the core fraction f_{core} allows us so mimic the fractal dimension, thus the lacyness of the BC aggregate, and its impact on the absorption and scattering cross section. The parameter R_1/R_{v} is meant to simulate the non-sphericity of the coating and its impact on polarimetric optical properties, especially depolarization.

We note that a much more complex dimer model was considered in [54] (see model 11 in that paper). The dimers in that model were composed of two encapsulated aggregates, each composed

Optics EXPRESS

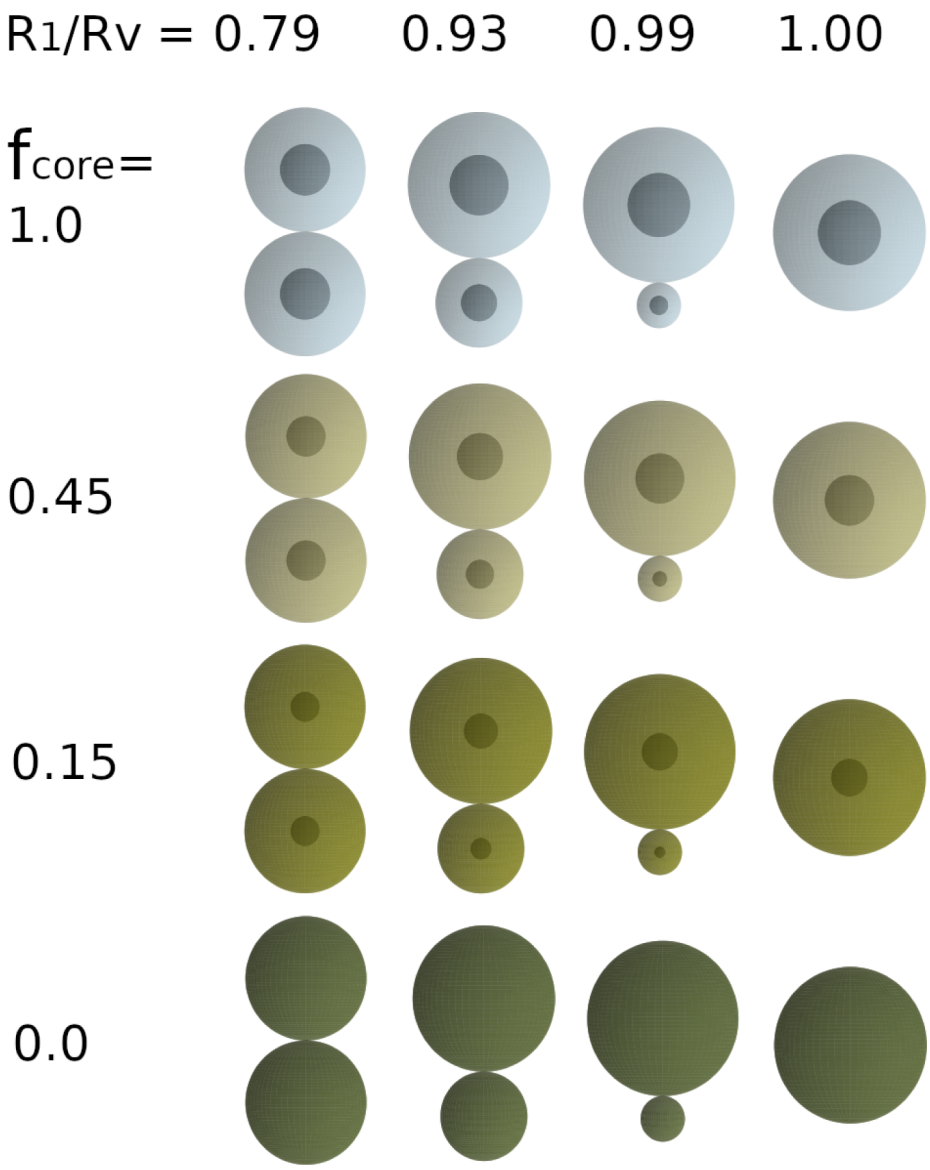

Fig. 3. Illustration of the CGS2 model and its two free parameters for a particle with a BC volume fraction of f_{BC}=0.07. The relative monomer size R_1/R_v varies among the columns, the BC core fraction f_{core} varies among rows. As the core fraction decreases, more BC is homogeneously mixed with the mantel. The corresponding change in the mantel's dielectric properties is represented by a change in color.

Optics EXPRESS

of a large number of monomers. However, neither the relative size of the dimers nor the fractal dimension of the aggregates were varied in [54]. Here, we will specifically study how the cross sections and depolarisation in our CGS2 model change in response to varying R_1/R_v and f_{core}.

2.2. Computational methods

We compute optical properties of randomly oriented particles. We are interested in the total extinction cross section, C_{ext}, the absorption cross section, C_{abs}, and the scattering cross section $C_{sca} = C_{ext} - C_{abs}$. In particular, the aerosol optical depth (AOD) depends on the aerosol number density, on C_{ext}, as well as on the vertical profiles of these two quantities. Further, we are interested in optical properties relevant to lidar remote sensing, i.e., in the backscattering cross section, C_{bak}, and the linear backscattering depolarization ratio, δ_l. The former is defined by

$$C_{bak} = \frac{1}{4\pi} C_{sca} F_{11}(180^\circ), \tag{4}$$

where the phase function F_{11} is the first element of the Stokes scattering matrix $F_{ij}(\Theta)$, where $i,j = 1,\ldots,4$. This matrix relates the four elements of the Stokes vector of the scattered field to those of the incident field in the scattering plane, and Θ denotes the scattering angle. The linear backscattering depolarisation ratio is defined by

$$\delta_l = \left. \frac{F_{11} - F_{22}}{F_{11} + 2F_{12} + F_{22}} \right|_{\Theta=180^\circ}. \tag{5}$$

We will consider ensembles of randomly oriented particles. In some cases, we will also consider ensembles of particles with different shapes. If we have an ensemble of particles of different types $m = 1, 2, \ldots$ with extinction cross sections $C_{ext}(m)$ and number density n_m, one computes ensemble-averages by taking the arithmetic mean of optical cross sections, e.g.

$$\bar{C}_{ext} = \frac{1}{N} \sum_m n_m \, C_{ext}(m), \tag{6}$$

where $N = \sum_m n_m$ is the total particle number density. Analogous expressions hold for C_{abs} and C_{sca}. The ensemble-averaged scattering matrix elements are computed according to

$$\bar{F}_{ij}(\Theta) = \frac{1}{\bar{C}_{sca}} \sum_m n_m \, C_{sca}(m) \, F_{ij,m}(\Theta), \tag{7}$$

where $F_{ij,m}$ is the (ij)-element of the scattering matrix of particle type m. The ensemble-averaged backscattering cross section and depolarisation ratio are computed by replacing C_{sca} and F_{ij} in Eqs. (4) and (5) with the corresponding ensemble-averages.

A variety of numerical methods can be used to compute optical properties of complex particles, such as coated aggregates (e.g. [63,64,68–70]). Here we briefly introduce the two codes that were employed in our study.

2.2.1. Amsterdam discrete dipole approximation (ADDA)

The reference calculations were performed using the DDA code ADDA (version 1.3b4) [71]. In order to solve the volume integral equation of the scattering problem with the help of the DDA the scatterer is divided into small, fully polarizable volume elements or dipoles. Dividing the scatterer into small dipoles leads to a set of linear equations, which can be solved with the help of numerical standard methods. Assuming the scatterer consisting of discrete dipoles allows the DDA to treat arbitrarily shaped and inhomogeneous particles [63,71].

The accuracy of DDA computations depends on the dipole spacing d and on the number of discrete angles employed in averaging over random orientations. There are extensive studies

Optics EXPRESS

published in the literature on testing the accuracy of the DDA with regard to these parameters, e.g. in [38,40,72]. Although even a fine dipole spacing can still yield DDA results that deviate from MSTM reference computations, we note that in our model the main source of uncertainty is the stochastic variation in the geometry. Thus the main requirement is that numerical errors in the DDA must be significantly smaller than the variation of the optical properties among different stochastic realisations of the aggregate geometry.

Here, we rely on uncertainty estimates for bare aggregates performed in [40], in which a dipole spacing given by $|m|kd = 0.43$ was recommended (where k is the wavenumber of light, and m is the complex refractive index of soot). This dipole spacing entails an uncertainty in the depolarization ratio that is one order of magnitude smaller than the uncertainty associated with stochastic variations of the fractal geometry. We use a dipole spacing $|m|kd = 0.24$, which is even more accurate than that recommended in [40]. Since each scatterer is assumed to be randomly orientated, ADDA's internal numerical orientation averaging is used. The orientation averaging is performed using discrete orientations. Following the calculations in [42] 1024 orientations are used for the orientation averaging. Further, the quasi minimal residual iterative solver QMR2 was employed and the scattering matrix elements were calculated with a angular resolution of 0.5°. Otherwise ADDA default settings were used.

2.2.2. Multiple sphere T matrix (MSTM)

The MSTM code [64] is based on iteratively solving an interaction equation for an arbitrary system of spherical surfaces. Each sphere is homogeneous, but different spheres can have different complex refractive indices. The only restriction is that the surfaces of the spheres must not overlap; any two spheres may share, at most, a single point. We use version 3.0 of the MSTM code, which has been adapted to parallel computing environments. The code computes orientation-averaged optical properties from the T-matrix by use of analytical solutions to the integration over Euler angles [73,74].

3. Results

3.1. Reference model

Table 1 presents optical properties computed with the reference model of coated BC aggregates. The rows present results for the four different cases of volume-equivalent radius and BC volume fraction (R_v,f_{BC}). The columns show results for $\bar{\delta}_l$, $\bar{C}_{bak}$, $\bar{C}_{ext}$, and $\bar{C}_{abs}$. Each optical property has been averaged over an ensemble of randomly oriented particles, over four values of the free parameter of the model, f_c, and over five stochastic realisations of the geometry for each value of f_c. For each optical property Q the values in parentheses denote the standard deviation

$$\sigma = \sqrt{\frac{1}{M}\sum_{m=1}^{M}(Q(m) - \bar{Q})^2}, \tag{8}$$

where the sum extends over the ensemble of $M = 20$ different geometries, i.e., over four different values of f_c and five different pseudo-random realisations of the geometry.

It is evident that for a given size R_v, $\bar{\delta}_l$ grows markedly with increasing f_{BC}. This can mainly be attributed to the significant differences in geometry, as illustrated in Fig. 1. We also observe that $\bar{C}_{abs}$ roughly doubles as we increase f_{BC} from 0.07 to 0.20, which is clearly caused by the increasing amount of absorbing material in the particle. $\bar{C}_{ext}$ also increases, but by an amount that is much larger for R_v=542nm than for 280nm. The increase in $\bar{C}_{abs}$ contributes to the growth of $\bar{C}_{ext}$. However, there are, most likely, oscillations in the size dependence of $\bar{C}_{sca}$ that enhance the growth of $\bar{C}_{ext}$ with increasing f_{BC} at 542nm, but depress its growth at 280 nm. Finally, we observe that $\bar{C}_{bak}$ is lowered as we increase f_{BC} from 0.07 to 0.20. All optical properties increase as the size grows from 280nm to 542nm.

Optics EXPRESS

Table 1. Reference results obtained with the irregular coated aggregate model. The entries show the ensemble-mean values, while the figures given in parentheses represent the standard deviations.

R_v	f_{BC}	$\bar{\delta}_l$	$\bar{C}_{bak}$ [$\mu m^2 sr^{-1}$]	$\bar{C}_{ext}$ [μm^2]	$\bar{C}_{abs}$ [μm^2]
0.542	0.07	0.073 (0.134)	0.0429 (0.0036)	2.609 (0.043)	0.745 (0.014)
0.542	0.20	0.103 (0.031)	0.0181 (0.0029)	4.310 (0.316)	1.486 (0.059)
0.280	0.07	0.005 (0.008)	0.0078 (0.0004)	0.732 (0.001)	0.129 (0.001)
0.280	0.20	0.055 (0.018)	0.0039 (0.0003)	0.787 (0.021)	0.258 (0.008)

Another notable point is the behavior of the standard deviation. For the cross sections, including $\bar{C}_{bak}$, σ is usually smaller than 10% of the mean value, in some cases even significantly smaller. By contrast, the standard deviation of $\bar{\delta}_l$ is at least 30% of the mean for f_{BC}=0.20, and up to 180% of the mean for f_{BC}=0.07. This is a result of the high sensitivity of the depolarisation ratio to a variation in geometry, and particularly to a distortion of the coating material. Owing to the large range of f_c-values used in our study, we obtain a considerable variability in geometries.

Why is the standard deviation of $\bar{\delta}_l$ so much higher for f_{BC}=0.07 than for 0.20? It is important to note that depolarisation is not a monotonic function of nonsphericity. For instance, it is well known that for weakly absorbing spheroids δ_l peaks for prolate spheroids that only deviate mildly from spherical shape [75]. Analogously, it has been demonstrated for the coated aggregate model that δ_l peaks if f_c is chosen such that the coating is only mildly nonspherical — see Fig. 7 and the accompanying discussion in [9]. We observe in Fig. 1 that for f_{BC}=0.07 our chosen range of f_c values is such that the coating is just in the vicinity of spherical shape, where δ_l can change most rapidly. By contrast, for f_{BC}=0.20 the coating is markedly nonspherical, yielding nonzero δ_l-values that are not as sensitive to a variation in geometry as they are in the proximity of spherical shape.

To simplify our notation, we will from here on drop the overbar over the ensemble-averaged optical properties.

3.2. Aggregate partially embedded in spherical coating

Figure 4 shows optical properties for the partially-embedded aggregate model as a function of the number of monomers inside the coating. C_{bak} (top right) and C_{ext} (bottom left) decrease almost monotonically with increasing N_s^{inside}, which can be understood in terms of a decreasing geometric cross section as more and more monomers of the aggregate are hidden inside the compact sphere of the coating material. By contrast, C_{abs} (bottom right) increases monotonically with growing N_s^{inside}, because the coating enhances the absorption by intercepting a larger amount of electromagnetic radiation than the amount that would be intercepted by a bare aggregate. This allows the embedded aggregate to absorb a larger amount of energy than it would absorb in its bare state. This well-known phenomenon is often referred to as the lensing effect, which is, arguably, a misinterpretative terminology, because it alludes to a geometric optics phenomenon, which does not really apply to the size-parameter regime we are dealing with here. δ_l first stagnates, then decreases with growing N_s^{inside} as the overall shape of the particle becomes more and more spherical. The model covers a δ_l-range of roughly 0.03–0.09.

3.3. CGS2 model

Figure 5 presents optical properties computed with the CGS2 model as a function of the model's two free parameters. The top row shows results for a particle of total radius R_v=542nm with a BC volume fraction f_{BC}=0.07. The results are represented by color shades. The most striking observation is that δ_l (top left) mainly depends on the nonsphericity parameter R_1/R_v (x-direction), while C_{abs} (top right) mainly depends on the BC core fraction f_{core} (y-direction). This is exactly

Optics EXPRESS

as intended; it means that for this particle we can adjust R_1/R_v and f_{core} independently to fit δ_l and C_{abs}, respectively. However, we will see shortly that for other particle sizes and BC volume fractions the situation may become more complex.

We want to adjust the free model parameters to simultaneously obtain a reasonable fit of not only δ_l and C_{abs}, but also C_{bak} and C_{ext}. To this end, we consider for each optical property Q_i the relative differences

$$\Delta Q_i = \frac{Q_i^{model} - Q_i^{ref}}{Q_i^{ref}}, \tag{9}$$

where the superscripts refer to the CGS2 model and the reference model, respectively, and where $Q_1 = \delta_l$, $Q_2 = C_{bak}$, $Q_3 = C_{ext}$, $Q_4 = C_{abs}$. We introduce the geometric mean error

$$\Delta = \sqrt{\frac{1}{4}\sum_{i=1}^{4}(\Delta Q_i)^2}. \tag{10}$$

This error metric is represented by the isolines in each panel of Fig. 5.

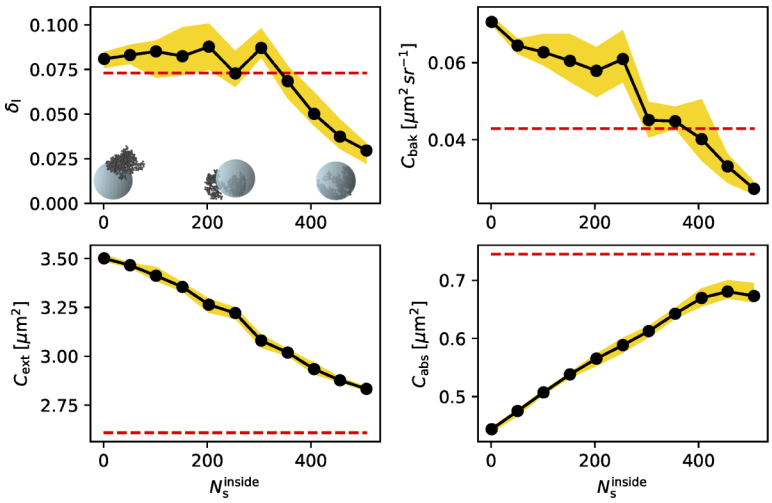

Fig. 4. δ_l (top left), C_{bak} (top right), C_{ext} (bottom left), and C_{abs} (bottom right) at a wavelength of 532 nm, computed with the partially-coated fractal aggregate model with spherical coating. The total number of monomers in the aggregate is N_s =508, and the x-axis shows the number of monomers inside the coating. The black curve shows the mean taken over 5 stochastic realisations of the geometry, the shading indicates the maximum and minimum values in the ensemble, and the dashed line represents the results obtained for the reference model.

We obtain the best simultaneous fit of all four optical parameters for model parameters around R_1/R_v=0.97 and f_{core}=0.3. This corresponds to dimers with rather unevenly sized monomers, i.e., not departing too much from a single monomer with R_1/R_v=1, and for particles in which 70% of the BC mass is homogeneously mixed with the coating.

It is also interesting to note that δ_l is not a simple monotonic function of the shape of the dimer. For spherically symmetric monomers (R_1/R_v=1) the depolarization is identically zero. As R_1/R_v is lowered, δ_l increases sharply and reaches a peak around R_1/R_v=0.92. C_{bak} has a minimum right around that value. When R_1/R_v is further reduced the depolarisation falls to about 0.2 and plateaus at that value.

To see the dependence of backscattering and depolarisation on the shape of the dimer more clearly, we show in Fig. 6 the scattering matrix elements F_{11} (left) and F_{22}/F_{11} (right) as functions

Optics EXPRESS

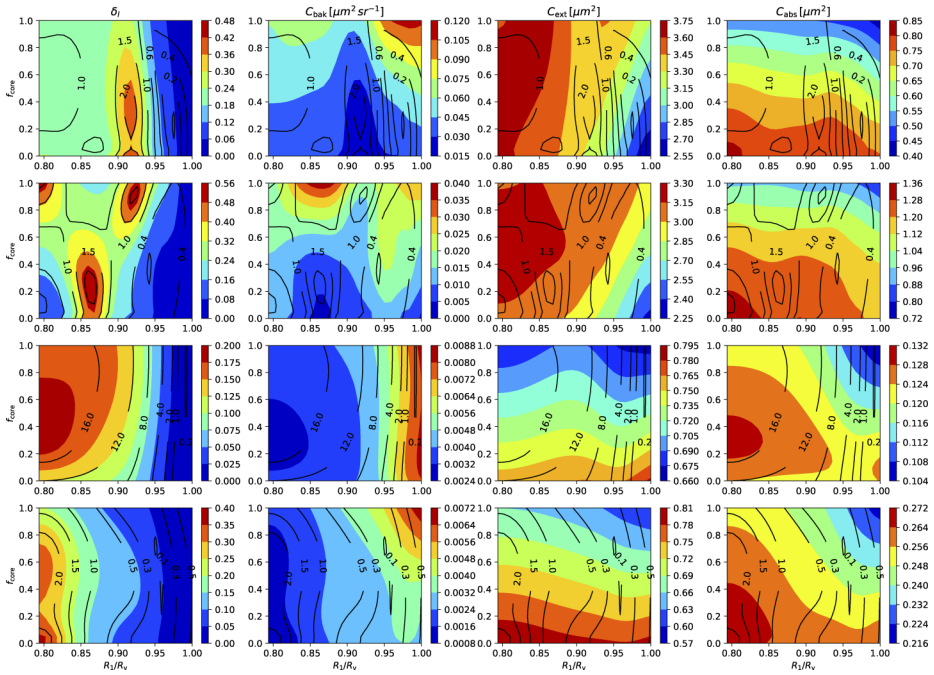

Fig. 5. δ_l (first column), $C_{\rm bak}$ (second column), $C_{\rm ext}$ (third column), and $C_{\rm abs}$ (fourth column) at a wavelength of 532 nm, as a function of the two free parameters in the CGS2 model. First row: $R_{\rm v}$ = 542 nm, $f_{\rm BC}$ =0.07; second row: $R_{\rm v}$ = 542 nm, $f_{\rm BC}$ = 0.20; third row: $R_{\rm v}$ = 0.280 μm, $f_{\rm BC}$ = 0.07; fourth row: $R_{\rm v}$ = 0.280 μm, $f_{\rm BC}$ = 0.20 The colour shadings represent the CGS2 model results, while the isolines indicate the deviation of the model from the reference computations as explained in the text.

of the scattering angle for four values of the dimer parameter $R_1/R_{\rm v}$, as indicated in the legend. As $R_1/R_{\rm v}$ increases from 0.79 up to 0.92, F_{11} and F_{22}/F_{11} decrease in the backscattering direction. This trend in both F_{11} and F_{22}/F_{11} is reversed as $R_1/R_{\rm v}$ is increased from 0.92 to 0.97. This closely reflects the corresponding behaviour of $C_{\rm bak}$ and δ_l in Fig. 5 (top row). (Note that a decrease in F_{22}/F_{11} entails an increase in δ_l and vice versa.)

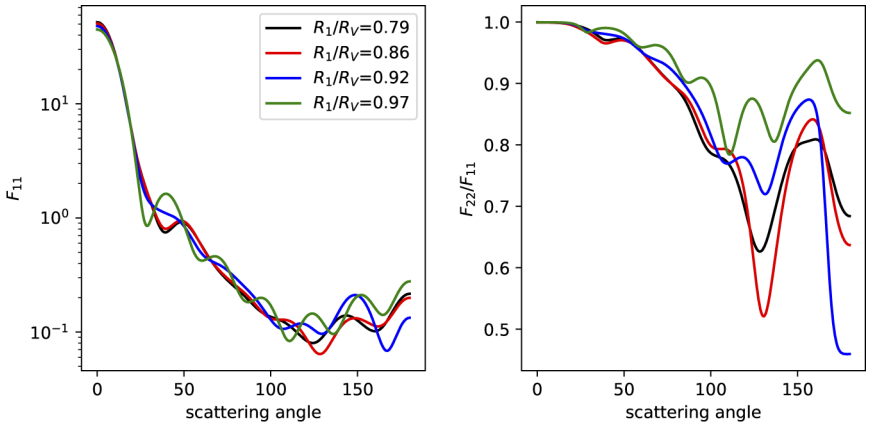

Fig. 6. F_{11} (left) and F_{22}/F_{11} for CGS2 particles with $R_{\rm v}$=542nm, $f_{\rm BC}$=0.07, and $f_{\rm core}$=0.5 for different values of $R_1/R_{\rm v}$ as indicated in the legend.

Optics EXPRESS

The second row in Fig. 5 shows analogous results for f_{BC}=0.20. Here, the picture becomes slightly more complex. δ_l still depends strongly on R_1/R_v, but we also see a dependence on f_{core}. C_{abs} is still mainly dependent on f_{core}, but it also displays a weak increase with decreasing R_1/R_v. However, as before the best fit of the reference results is achieved for relatively high values of R_1/R_v and low values of f_{core}. As in in the top row, the minimum of Δ is fairly broad in the y-direction, and much narrower in the x-direction. In the region of interest around the error minimum δ_l displays a strong dependency on R_1/R_v, and only a very weak dependency on f_{core}. The third row shows similar results, but for R_v=280nm and f_{BC}=0.07. The best fit is achieved for R_1/R_v around 0.98. Again, for R_1/R_v>0.9 the depolarisation is essentially independent of f_{core}. The minimum of Δ is very broad in the y-direction. A comparison with Table 1 shows that at R_1/R_v around 0.98 C_{bak} is best represented by high values of f_{core}, C_{ext} by intermediate values of f_{core}, and C_{abs} by low values of f_{core}.

The fourth row shows results for R_v=280nm and f_{BC}=0.20. The isolines indicate that Δ has a minimum around R_1/R_v=0.96 which is, again, very broad in the y-direction.

By comparing the scale of C_{ext} to C_{abs} in each of the four rows, we see that scattering always makes the dominant contribution to the total extinction cross section. A curious observation is that for R_v=542nm extinction is strongly dependent on R_1/R_v, and only weakly dependent on f_{core} (rows 1 and 2, third column). For R_v=280nm (rows 3 and 4, third column), this is reversed. Since extinction is dominated by scattering, and since C_{abs} does not display such a reversal, we conclude that for small particles scattering is strongly dependent on the dielectric properties of the coating, while for large particles it becomes mostly dependent on the shape of the dimer.

4. Discussion

In Sec. 3.2, specifically in Fig. 3, we presented computations performed with the partially embedded aggregate model with a spherical coating. The results reveal some of the main weaknesses of the model.

- **Range of δ_l-values**. The range of depolarization ratios is limited to $\delta_l \leq 0.09$. In the literature one finds reported values based on field observations in the range 0.015–0.23, although the majority of reported values lie below 0.11 (see Table 11 in [41]). Note that field measurements observe size-averaged values. The particles considered in Fig. 4 are relatively large. For smaller particles, it is likely that the model will yield even lower depolarization ratios. Therefore, for typical size distributions of coated BC aerosols this model is expected to give δ_l-values that lie in the lower range of reported literature values. This considerably narrows down the potential usefulness of the model.

- **Model flexibility**. The main idea of this model was to find a way to tune the depolarisation ratio. However, we see in Fig. 3 that a variation of the model's free parameter, N_s^{inside}, impacts not only δ_l, but also the optical cross sections. This makes it difficult to find a setting of N_s^{inside} that works well for all optical properties. For δ_l, the agreement of the model with the reference computations is best for $N_s^{inside} \leq 350$, but for C_{bak} we obtain the best agreement for $N_s^{inside} \approx 400$.

- **Scope of model application**. The model seems to work for differential scattering properties, but it fails to give a good representation of the integral optical properties. The reference value of C_{ext} is consistently overestimated, that of C_{abs} is systematically underestimated. A possible cause may be the differences in the numerical construction of the fractal aggregates. In the reference model, the fractal scaling law in Eq. (1) was the only condition that constrained the geometry while assembling the aggregates. By contrast, in the partially embedded aggregate model both the scaling law as well as the condition that the embedded part of the aggregate be fully contained within the coating

Optics EXPRESS

constrained the aggregate geometry. Further, the reference particles were constructed by use of the cluster-cluster aggregation algorithm [62], in which smaller aggregates are assembled into larger aggregates. This method mimics the aggregation process by which real aggregates are formed in combustion processes. By contrast, the partially embedded aggregates were assembled by use of the diffusion-limited aggregation algorithm [65], in which one monomer at a time is added to the aggregate. In the latter algorithm it is easier to comply with the rather strict constraint that the embedded portion of the aggregate is fully encapsulated by the coating. It is likely that these differences in the aggregates' construction method give rise to overall more compact fractal structures in the partially embedded particles. More densely packed monomers will more strongly interact with each other, which can enhance the scattering cross section. On the other hand, they will also shield one another more efficiently, resulting in a reduction in the absorbed energy. This is one plausible explanation for the underestimation of C_{abs} and the overestimation of C_{sca} by this model.

These findings are consistent with results reported in [10], in which an MSTM-based coated aggregate model with partially embedded aggregates of non-overlapping spheres with spherical coating was considered. Although depolarization is not specifically discussed there, inspection of Figs. 4, 5, 8, and 9 in Ref. [10] reveals that the F_{22}/F_{11} element of the scattering matrix varies only within a fairly narrow range close to 1, which will translate into a limited range of low depolarization ratios — see Eq. (5). Similar to our study, this can be attributed to the sphericity of the coating.

The spherical coating model gives a lidar ratio (proportional to $C_{\mathrm{ext}}/C_{\mathrm{bak}}$) that agrees with the reference model at about N_s=280 (not shown). Inspection of Fig. 4 shows that at this point the model overestimates C_{ext} and C_{bak} by an equal amount. Thus, this model allows us to correctly model the lidar ratio only at the expense of misrepresenting both the backscattering and the extinction cross section.

Owing to the shortcomings of the spherical-coating assumption, we have to dismiss this model for our purposes. The most important observation is that this model only covers a limited range of depolarization ratios. This may be interpreted as an indirect corroboration of earlier claims [9,40–42] according to which the nonsphericity of the coating is the most important morphological property that determines the depolarisation ratio of coated BC aerosols.

However, even more convincing evidence for this hypothesis comes from the CGS2 model. The tests of that model reveal the following properties.

- **Range of δ_l-values**. In the CGS2 model, thanks to the nonsphericity of the coating, the depolarisation ratio varies over a considerable range. For R_{v}=280nm and f_{BC}=0.07, the model covers a range of δ_l=0–0.2. In all other cases that range is extended up to more than 0.40. This clearly braces, and even exceeds the range of typical values observed in field observations.

- **Model flexibility**. The model possesses two free parameters. The depolarization ratio can mainly be tuned by varying R_1/R_{v}, while the absorption cross section strongly depends on f_{core}.

- **Scope of model application**. The results in Fig. 5 show that it is possible to attain a reasonably good fit of δ_l, C_{bak}, C_{ext}, and C_{abs} by an appropriate choice of R_1/R_{v} and f_{core}. This makes this model particularly interesting in applications such as chemical data assimilation of both lidar and AOD observations.

These observations are based on a comparison of the model to four references cases, characterized by two different particle radii and two different BC volume fractions. In our attempt to

Optics EXPRESS

simultaneously fit δ_l, C_{bak}, C_{ext}, and C_{abs} we obtain rather concordant results. In all cases we obtained the best agreement between the CGS2 model and the reference results for R_1/R_{v} in the range 0.94–0.98, i.e., for CGS dimers of rather unevenly sized monomers. The exact choice of the BC core fraction is less critical; the minimum of the error is fairly broad in the f_{core}-direction. In most cases values of f_{core} around 0.5 or less seem to give the best agreement with the reference values.

Incidentally, these results seem to be rather robust with regard to the choice of error metric. We also tested a root mean square (rms) error metric, in which Eq. (9) is replaced by

$$\Delta Q_i = \frac{Q_i^{\mathrm{model}} - Q_i^{\mathrm{ref}}}{\sigma_i}, \tag{11}$$

where σ_i denotes the standard deviations of the reference model results given in Table 1. Owing to the high standard deviation of the δ_l reference values, this metric puts less emphasis on the depolarisation ratio and more emphasis on the cross sections. Despite these differences, it turns out (not shown) that this rms error metric has a minimum around R_1/R_{v}=0.94–0.98, just like the geometric mean error given in Eq. (10). The main difference is that the minimum is less broad in the f_{core}-direction; it is more concentrated around f_{core}<0.5.

In Fig. 5 we tried to fit reference computations for a particle of definite size and BC volume fraction. In more realistic applications we will need to fit optical properties of size distributions, which is almost always easier than fitting optical properties of single particles. The fact that our model consistently yielded the best agreement with the reference results for similar choices of the model's free parameters is very encouraging. There are good prospects that this model will be able to represent the optical properties of size distributions of coated BC aerosols over a range of relevant size distributions and BC volume fractions.

Finally, a remark on the CPU time requirements is in order. The simplicity of the CGS2 model results in low computational demands, which makes this model suitable for building extensive look-up tables for remote sensing retrieval algorithms, chemical data assimilation systems, or radiation schemes in climate models. Note that the MSTM code employed here has been developed for aggregates of arbitrary shape. Thus this code has no provisions to systematically exploit the axial symmetry of the CGS2 dimers. The use of geometric symmetry can drastically reduce computational requirements in T-matrix computations by orders of magnitude [76,77]. Thus, if required, the CPU time needed for the CGS2 model could even be further reduced substantially.

5. Conclusions

We embarked on this work in search of a light scattering model of coated BC particles that could be used in large-scale applications. Such applications set tight constraints on computational speed, which often necessitates drastic simplifications. Such requirements are very difficult to reconcile with the intricate morphological properties of real BC aerosols. This becomes even more challenging for polarimetric optical properties, which can be highly sensitive to even minor morphological subtleties. Thus an important question is how much morphological details we can leave out in a model without sacrificing our ability to simulate radiometric and polarimetric properties.

The partially embedded aggregate model in Fig. 2 is morphologically reasonably realistic. It incorporates the fractal aggregate morphology of real BC aerosols, as well as their partial embedding into liquid coating material. However, it only accounts for spherical coatings. This is likely to be the main reason why this model is too restricted in the range of δ_l values that it can reproduce. Owing to this limitation, we have to dismiss this model for the purpose of modelling depolarisation by coated BC aerosols.

Optics EXPRESS

We devised a new model, shown in Fig. 3, which we labeled the CGS2 model. This is a model specifically intended for large-scale applications, in which the morphological features of BC aerosols are trimmed down to the bare essentials. The main idea in the CGS2-model is to modify the conventional CGS model [39] by making the shape nonspherical. The main hypothesis is that the single most important morphological characteristic that determines δ_l is the shape of the weakly absorbing coating. Clearly our reference model already possessed that capability. However, that model is computationally very demanding. The proposed solution is to assemble two CGS spheres into a dimer. The relative size of the two monomers, expressed by the parameter R_1/R_v, as well as the core fraction of BC, f_{core}, are the two free parameters of the model.

The results are consistent with our hypothesis. The CGS2 model does, indeed, cover a considerable range of depolarization ratios that braces the range of typical values observed in lidar field measurements. The depolarization ratio can mainly be tuned by varying R_1/R_v, while the absorption cross section strongly depends on f_{core}. We conclude that the CGS2 model, despite being based on drastic morphological simplifications, can capture the main features of coated BC particles and their impact on optical properties, namely, (i) the compactness of the distribution of the BC mass within the inhomogeneous particle and its impact on cross sections; and (ii) the deviation from spherical shape of the coating and its impact on depolarisation.

In our attempt to reproduce the reference results, a fairly consistent picture emerged. In all four test cases, the CGS2 model yielded the best agreement with the reference results for R_1/R_v in the range 0.94–0.98, and for $f_{core} \leq 0.5$. If these observations should hold over a broader range of particle sizes and BC volume fractions, then it should be straightforward to generalize this model to size distributions of aerosols. We conclude that the CGS2 model has the potential of bringing us closer to a simple yet consistent description of aerosol optical properties for large-scale environmental applications. Together with recent progress on mineral dust [78] and sea salt [79,80] we may soon be in a position to compile an aerosol-optics data base of radiometric and polarimetric properties that can be applied to general circulation models, remote sensing retrieval methods, and chemical data assimilation.

A final point needs to be stressed to preclude any misunderstandings about our main conclusions. The question whether a model particle is useful or not consists of two very distinct parts that must not be confused with each other. The first part concerns a model class, the second one concerns a class instance. In our case, the first part of the question is whether or not the CGS2 *class* of model particles, illustrated in Fig. 3, is sufficiently flexible to simulate radiometric and polarimetric observations of coated BC aerosols. The second part of the question is whether or not a specific *instance* of this model class, characterized by R_1/R_v in the range 0.94–0.98 and f_{core} around 0.5, is likely to give the best representation of the optical properties. Our findings, so far, are very promising with regard to the first part of the question. It remains to be seen if the usefulness of the CGS2 class of model particles can be generalized from the visible to other wavelengths in the UV and NIR. The conclusions pertaining to the second part of the question were based on a comparison with a specific reference model. As more detailed reference information will become available, preferably from measurements, the specific tuning of the model will need to be revisited and refined. Thus, both parts of the question are open to further scrutiny.

Funding. Vetenskapsrådet (2016-03499); Swedish National Space Agency (126/19).

Acknowledgments. Maxim Yurkin and Alfons Hoekstra are acknowledged for making their ADDA code publicly available. We are also grateful to Dan Mackowski for making his MSTM program publicly available, and for giving us access to his aggregate aggregation code.

Disclosures. The authors declare no conflicts of interest.

Data Availability. Data underlying the results presented in this paper are publicly available in Ref. [81].

References

1. V. Ramanathan and G. Carmichael, "Global and regional climate changes due to black carbon," Nat. Geosci. **1**(4), 221–227 (2008).

Optics EXPRESS

2. G. Myhre, D. Shindell, F.-M. Bréon, W. Collins, J. Fuglestvedt, J. Huang, D. Koch, J.-F. Lamarque, D. Lee, B. Mendoza, T. Nakajima, A. Robock, G. Stephens, T. Takemura, and H. Zhang, *Anthropogenic and Natural Radiative Forcing* (Cambridge University, 2013), Cambridge, United Kingdom, book section 8, pp. 659–740.
3. T. C. Bond, S. J. Doherty, D. W. Fahey, P. M. Forster, T. Berntsen, B. J. DeAngelo, M. G. Flanner, S. Ghan, B. Kärcher, D. Koch, S. Kinne, Y. Kondo, P. K. Quinn, M. C. Sarofim, M. G. Schultz, M. Schulz, C. Venkataraman, H. Zhang, S. Zhang, N. Bellouin, S. K. Guttikunda, P. K. Hopke, M. Z. Jacobson, J. W. Kaiser, Z. Klimont, U. Lohmann, J. P. Schwarz, D. Shindell, T. Storelvmo, S. G. Warren, and C. S. Zender, "Bounding the role of black carbon in the climate system: A scientific assessment," J. Geophys. Res. **118**(11), 5380–5552 (2013).
4. S. C. Anenberg, J. Schwartz, D. Shindell, M. Amann, G. Faluvegi, Z. K. G. Janssens-Maenhout, L. Pozzoli, R. V. Dingenen, E. Vignati, L. Emberson, N. Z. Muller, J. J. West, M. Williams, V. Demkine, W. K. Hicks, J. Kuylenstierna, F. Raes, and V. Ramanathan, "Global air quality and health co-benefits of mitigating near-term climate change through methane and black carbon emission controls," Environ. Health Perspect. **120**(6), 831–839 (2012).
5. M. Z. Jacobson, "A physically-based treatment of elemental carbon optics: Implications for global direct forcing of aerosols," Geophys. Res. Lett **27**(2), 217–220 (2000).
6. M. Kahnert, "Numerically exact computation of the optical properties of light absorbing carbon aggregates for wavelength of 200 nm – 12.2 μm," Atmos. Chem. Phys. **10**(17), 8319–8329 (2010).
7. M. Kahnert and A. Devasthale, "Black carbon fractal morphology and short-wave radiative impact: a modelling study," Atmos. Chem. Phys. **11**(22), 11745–11759 (2011).
8. C. Zeng, C. Liu, J. Li, B. Zhu, Y. Yin, and Y. Wang, "Optical properties and radiative forcing of aged bc due to hygroscopic growth: Effects of the aggregate structure," J. Geophys. Res. **124**(8), 4620–4633 (2019).
9. M. Kahnert and F. Kanngießer, "Modelling optical properties of atmospheric black carbon aerosols," J. Quant. Spectrosc. Radiat. Transfer **244**, 106849 (2020).
10. C. Liu, J. Li, Y. Yin, B. Zhu, and Q. Feng, "Optical properties of black carbon aggregates with non-absorptive coating," J. Quant. Spectrosc. Radiat. Transfer **187**, 443–452 (2017).
11. C. Liu, "Optical properties of black carbon aggregates," in *Springer Series in Light Scattering: Volume 3: Radiative Transfer and Light Scattering*, A. Kokhanovsky, ed. (Springer International Publishing, 2019), Cham, pp. 167–218.
12. C. He, "Radiative properties of atmospheric black carbon (soot) particles with complex structures," in *Springer Series in Light Scattering: Volume 4: Light Scattering and Radiative Transfer*, A. Kokhanovsky, ed. (Springer International Publishing, 2019), Cham, pp. 219–254.
13. R. Ceolato, L. Paulien, J. B. Maughan, C. M. Sorensen, and M. J. Berg, "Radiative properties of soot fractal superaggregates including backscattering and depolarization," J. Quant. Spectrosc. Radiat. Transfer **247**, 106940 (2020).
14. A. Smekens, J. Pauwels, P. Berghmans, and R. V. Grieken, "Correlation study between the aerodynamic diameter and the number of primary particles of soot aggregates by STEM," J. Aerosol Sci. **28**, S761–S762 (1997).
15. J. Li, J. R. Anderson, and P. R. Buseck, "TEM study of aerosol particles from clean and polluted marine boundary layers over the North Atlantic," J. Geophys. Res. **108**(D6), 2002JD002106 (2003).
16. K. Adachi and P. R. Buseck, "Internally mixed soot, sulfates, and organic matter in aerosol particles from Mexico City," Atmos. Chem. Phys. **8**(21), 6469–6481 (2008).
17. K. Adachi, S. Chung, and P. R. Buseck, "Shapes of soot aerosol particles and implications for their effects on climate," J. Geophys. Res. **115**(D15), D15206 (2010).
18. M. Schnaiter, C. Linke, O. Moehler, K.-H. Naumann, H. Saathoff, R. Wagner, U. Schurath, and B. Wehner, "Absorption amplification of black carbon internally mixed with secondary organic aerosol," J. Geophys. Res. **110**(D19), D19204 (2005).
19. M. Shiraiwa, Y. Kondo, T. Iwamoto, and K. Kita, "Amplification of light absorption of black carbon by organic coating," Aerosol Sci. Technol. **44**(1), 46–54 (2010).
20. E. F. Mikhailov, S. S. Vlasenko, I. A. Podgorny, V. Ramanathan, and C. E. Corrigan, "Optical properties of soot-water drop agglomerates: An experimental study," J. Geophys. Res. **111**(D7), D07209 (2006).
21. C. Liu, R. L. Panetta, P. Yang, A. Macke, and A. J. Baran, "Modeling the scattering properties of mineral aerosols using concave fractal polyhedra," Appl. Opt. **52**(4), 640–652 (2013).
22. M. I. Mishchenko, L. Liu, B. Cairns, and D. W. Mackowski, "Optics of water cloud droplets mixed with black-carbon aerosols," Opt. Lett. **39**(9), 2607–2610 (2014).
23. T. Cheng, X. Gu, Y. Wu, and H. Chen, "Effects of atmospheric water on the optical properties of soot aerosols with different mixing states," J. Quant. Spectrosc. Radiat. Transfer **147**, 196–206 (2014).
24. M. Kahnert, "On the discrepancy between modelled and measured mass absorption cross sections of light absorbing carbon aerosols," Aerosol Sci. Technol. **44**(6), 453–460 (2010).
25. T. L. Farias, Ü. Ö. Köylü, and M. G. Carvalho, "Effects of polydispersity of aggregates and primary particles on radiative properties of simulated soot," J. Quant. Spectrosc. Radiat. Transfer **55**(3), 357–371 (1996).
26. L. Liu, M. I. Mishchenko, and W. P. Arnott, "A study of radiative properties of fractal soot aggregates using the superposition *T*-matrix method," J. Quant. Spectrosc. Radiat. Transfer **109**(15), 2656–2663 (2008).
27. C. Liu, Y. Yin, F. Hu, H. Jin, and C. M. Sorensen, "The effect of monomer size distribution on the radiative properties of black carbon aggregates," Aerosol Sci. Technol. **49**(10), 928–940 (2015).
28. Y. Wu, T. Cheng, L. Zheng, and H. Chen, "A study of optical properties of soot aggregates composed of poly-disperse monomers using the superposition T-matrix method," Aerosol Sci. Technol. **49**(10), 941–949 (2015).

Optics EXPRESS

29. N. Doner and F. Liu, "Impact of morphology on the radiative properties of fractal soot aggregates," J. Quant. Spectrosc. Radiat. Transfer **187**, 10–19 (2017).
30. Y. Wu, T. Cheng, L. Zheng, and H. Chen, "Effect of morphology on the optical properties of soot aggregated with spheroidal monomers," J. Quant. Spectrosc. Radiat. Transfer **168**, 158–169 (2016).
31. C. Oh and C. M. Sorensen, "The effect of overlap between monomers on the determination of fractal cluster morphology," J. Colloid Interface Sci. **193**(1), 17–25 (1997).
32. A. Bescond, J. Yon, T. Girasole, C. Jouen, C. Rozé, and A. Coppalle, "Numerical investigation of the possibility to determine the primary particle size of fractal aggregates by measuring light depolarization," J. Quant. Spectrosc. Radiat. Transfer **126**, 130–139 (2013).
33. K. Skorupski, J. Mroczka, N. Riefler, H. Oltmann, S. Will, and T. Wriedt, "Impact of morphological parameters onto simulated light scattering patterns," J. Quant. Spectrosc. Radiat. Transfer **119**, 53–66 (2013).
34. K. Skorupski and J. Mroczka, "Effect of the necking phenomenon on the optical properties of soot particles," J. Quant. Spectrosc. Radiat. Transfer **141**, 40–48 (2014).
35. J. Yon, A. Bescond, and F. Liu, "On the radiative properties of soot aggregates part 1: Necking and overlapping," J. Quant. Spectrosc. Radiat. Transfer **162**, 197–206 (2015).
36. S. Teng, C. Liu, M. Schnaiter, R. K. Chakrabarty, and F. Liu, "Accounting for the effects of nonideal minor structures on the optical properties of black carbon aerosols," Atmos. Chem. Phys. **19**(5), 2917–2931 (2019).
37. A. Worringen, M. Ebert, T. Trautmann, S. Weinbruch, and G. Helas, "Optical properties of internally mixed ammonium sulfate and soot particles–a study of individual aerosol particles and ambient aerosol populations," Appl. Opt. **47**(21), 3835–3845 (2008).
38. M. Kahnert, T. Nousiainen, H. Lindqvist, and M. Ebert, "Optical properties of light absorbing carbon aggregates mixed with sulfate: assessment of different model geometries for climate forcing calculations," Opt. Express **20**(9), 10042–10058 (2012).
39. M. Kahnert, T. Nousiainen, and H. Lindqvist, "Models for integrated and differential scattering optical properties of encapsulated light absorbing carbon aggregates," Opt. Express **21**(7), 7974–7992 (2013).
40. M. Kahnert, "Optical properties of black carbon aerosols encapsulated in a shell of sulphate: comparison of the closed cell model with a coated aggregate model," Opt. Express **25**(20), 24579–2493 (2017).
41. F. Kanngießer and M. Kahnert, "Calculation of optical properties of light-absorbing carbon with weakly absorbing coating: A model with tunable transition from film-coating to spherical-shell coating," J. Quant. Spectrosc. Radiat. Transfer **216**, 17–36 (2018).
42. F. Kanngießer and M. Kahnert, "Coating material-dependent differences in modelled lidar-measurable quantities for heavily coated soot particles," Opt. Express **27**(25), 36368–36387 (2019).
43. H. Ishimoto, R. Kudo, and K. Adachi, "A shape model of internally mixed soot particles derived from artificial surface tension," Atmos. Meas. Tech. **12**(1), 107–118 (2019).
44. C. Liu, X. Xu, Y. Yin, M. Schnaiter, and Y. L. Yung, "Black carbon aggregates: A database for optical properties," J. Quant. Spectrosc. Radiat. Transfer **222-223**, 170–179 (2019).
45. M. Kahnert, "Modelling the optical and radiative properties of freshly emitted light absorbing carbon within an atmospheric chemical transport model," Atmos. Chem. Phys. **10**(3), 1403–1416 (2010).
46. B. Scarnato, S. Vahidinia, D. T. Richard, and T. W. Kirchstetter, "Effects of internal mixing and aggregate morphology on optical properties of black carbon using a discrete dipole approximation model," Atmos. Chem. Phys. **13**(10), 5089–5101 (2013).
47. J. Dong, J. M. Zhao, and L. H. Liu, "Morphological effects on the radiative properties of soot aerosols in different internally mixing states with sulfate," J. Quant. Spectrosc. Radiat. Transfer **165**, 43–55 (2015).
48. Y. Wu, T. Cheng, L. Zheng, H. Chen, and H. Xu, "Single scattering properties of semi-embedded soot morphologies with intersecting and non-intersecting surfaces of absorbing spheres and non-absorbing host," J. Quant. Spectrosc. Radiat. Transfer **157**, 1–13 (2015).
49. F. Liu, J. Yon, and A. Bescond, "On the radiative properties of soot aggregates — Part 2: Effects of coating," J. Quant. Spectrosc. Radiat. Transfer **172**, 134–145 (2016).
50. Y. Wu, T. Cheng, L. Zheng, and H. Chen, "Sensitivity of mixing states on optical properties of fresh secondary organic carbon aerosols," J. Quant. Spectrosc. Radiat. Transfer **195**, 147–155 (2017).
51. X. Zhang, M. Mao, Y. Yin, and B. Wang, "Absorption enhancement of aged black carbon aerosols affected by their microphysics: A numerical investigation," J. Quant. Spectrosc. Radiat. Transfer **202**, 90–97 (2017).
52. Y. Wu, T. Cheng, D. Liu, J. D. Allan, L. Zheng, and H. Chen, "Light absorption enhancement of black carbon aerosol constrained by particle morphology," Environ. Sci. Technol. **52**(12), 6912–6919 (2018). PMID: 29783837.
53. J. Luo, Y. Zhang, F. Wang, and Q. Zhang, "Effects of brown coatings on the absorption enhancement of black carbon: a numerical investigation," Atmos. Chem. Phys. **18**(23), 16897–16914 (2018).
54. L. Liu and M. I. Mishchenko, "Scattering and radiative properties of morphologically complex carbonaceous aerosols: A systematic modeling study," Remote Sens. **10**(10), 1634 (2018).
55. R. K. Chakrabarty and W. R. Heinson, "Scaling laws for light absorption enhancement due to nonrefractory coating of atmospheric black carbon aerosol," Phys. Rev. Lett. **121**(21), 218701 (2018).
56. E. Andersson and M. Kahnert, "Coupling aerosol optics to the MATCH (v5. 5.0) chemical transport model and the SALSA (v1) aerosol microphysics module," Geosci. Model Dev. **9**(5), 1803–1826 (2016).

Optics EXPRESS

57. M. Kahnert and E. Andersson, "How much information do extinction and backscattering measurements contain about the chemical composition of atmospheric aerosol," Atmos. Chem. Phys. **17**(5), 3423–3444 (2017).
58. A. Gialitaki, A. Tsekeri, V. Amiridis, R. Ceolato, L. Paulien, A. Kampouri, A. Gkikas, S. Solomos, E. Marinou, M. Haarig, H. Baars, A. Ansmann, T. Lapyonok, A. Lopatin, O. Dubovik, S. Groß, M. Wirth, M. Tsichla, I. Tsikoudi, and D. Balis, "Is the near-spherical shape the "new black" for smoke?" Atmos. Chem. Phys. **20**(22), 14005–14021 (2020).
59. M. A. Thomas, M. Kahnert, C. Andersson, H. Kokkola, U. Hansson, C. Jones, J. Langner, and A. Devasthale, "Integration of prognostic aerosol–cloud interactions in a chemistry transport model coupled offline to a regional climate model," Geosci. Model Dev. **8**(6), 1885–1898 (2015).
60. H. Chang and T. T. Charalampopoulos, "Determination of the wavelength dependence of refractive indices of flame soot," Proc. R. Soc. Lond. A **430**(1880), 577–591 (1990).
61. M. Hess, P. Koepke, and I. Schult, "Optical properties of aerosols and clouds: The software package OPAC," Bull. Am. Meteorol. Soc. **79**(5), 831–844 (1998).
62. D. W. Mackowski, "Calculation of total cross sections of multiple-sphere clusters," J. Opt. Soc. Am. A **11**(11), 2851–2861 (1994).
63. M. A. Yurkin and A. G. Hoekstra, "The discrete dipole approximation: An overview and recent developments," J. Quant. Spectrosc. Radiat. Transfer **106**(1-3), 558–589 (2007).
64. D. W. Mackowski and M. I. Mishchenko, "A multiple sphere T-matrix Fortran code for use on parallel computer clusters," J. Quant. Spectrosc. Radiat. Transfer **112**(13), 2182–2192 (2011).
65. C. M. Sorensen and G. M. Roberts, "The prefactor of fractal aggregates," J. Colloid Interface Sci. **186**(2), 447–452 (1997).
66. P. Chýlek, G. Videen, D. J. W. Geldart, J. S. Dobbie, and H. C. W. Tso, "Effective medium approximations for heterogeneous particles," in *Light scattering by nonspherical particles*, M. I. Mishchenko, J. W. Hovenier, and L. D. Travis, eds. (Academic Press, 2000), San Diego, pp. 274–308.
67. A. Quirantes, "A t-matrix method and computer code for randomly oriented, axially symmetric coated scatterers," J. Quant. Spectrosc. Radiat. Transfer **92**(3), 373–381 (2005).
68. Y. Takano, K. N. Liou, M. Kahnert, and P. Yang, "The single-scattering properties of black carbon aggregates determined from the geometric-optics surface-wave approach and the t-matrix method," J. Quant. Spectrosc. Radiat. Transfer **125**, 51–56 (2013).
69. L. Bi, P. Yang, G. W. Kattawar, and M. I. Mishchenko, "Efficient implementation of the invariant imbedding t-matrix method and the separation of variables method applied to large nonspherical inhomogeneous particles," J. Quant. Spectrosc. Radiat. Transfer **116**, 169–183 (2013).
70. B. Sun, L. Bi, P. Yang, M. Kahnert, and G. Kattawar, *Invariant Imbedding T-matrix Method for Light Scattering by Nonspherical and Inhomogeneous Particles* (Elsevier, 2019), Amsterdam.
71. M. A. Yurkin and A. G. Hoekstra, "The discrete-dipole-approximation code ADDA: Capabilities and known limitations," J. Quant. Spectrosc. Radiat. Transfer **112**(13), 2234–2247 (2011).
72. C. Liu, S. Teng, Y. Zhu, M. A. Yurkin, and Y. L. Yung, "Performance of the discrete dipole approximation for optical properties of black carbon aggregates," J. Quant. Spectrosc. Radiat. Transfer **221**, 98–109 (2018).
73. N. G. Khlebtsov, "Orientational averaging of light-scattering observables in the T-matrix approach," Appl. Opt. **31**(25), 5359–5365 (1992).
74. D. W. Mackowski and M. I. Mishchenko, "Calculation of the T matrix and the scattering matrix for ensembles of spheres," J. Opt. Soc. Am. A **13**(11), 2266–2278 (1996).
75. M. I. Mishchenko and J. W. Hovenier, "Depolarization of light backscattered by randomly oriented nonspherical particles," Opt. Lett. **20**(12), 1356–1358 (1995).
76. F. M. Schulz, K. Stamnes, and J. J. Stamnes, "Point group symmetries in electromagnetic scattering," J. Opt. Soc. Am. A **16**(4), 853–865 (1999).
77. M. Kahnert, "Irreducible representations of finite groups in the T matrix formulation of the electromagnetic scattering problem," J. Opt. Soc. Am. A **22**(6), 1187–1199 (2005).
78. M. Kahnert, F. Kanngießer, E. Järvinen, and M. Schnaiter, "Aerosol-optics model for the backscatter depolarisation ratio of mineral dust particles," J. Quant. Spectrosc. Radiat. Transfer **254**, 107177 (2020).
79. L. Bi, W. Lin, D. Liu, and K. Zhang, "Assessing the depolarization capabilities of nonspherical particles in super-ellipsoidal shape space," Opt. Express **26**(2), 1726–1742 (2018).
80. F. Kanngießer and M. Kahnert, "Modeling optical properties of non-cubical sea-salt particles," J. Geophyys. Res. **126**(4), e2020JD033674 (2021).
81. M. Kahnert and F. Kanngießer, "Black carbon optical properties (version 1.0) [data set]," Zenodo. http://doi.org/10.5281/zenodo.4507029

38.128.187.71 {ts '2021-04-16 03:31:50'}